INTERNATIONAL JOURNAL FOR NUMERICAL METHODS IN FLUIDS, VOL. 21, 699–722 (1995)

VISCOUS–INVISCID COUPLING IN FREE SURFACE SHIP FLOWS

E. CAMPANA, A. DI MASCIO, P. G. ESPOSITO AND F. LALLI

Istituto Nazionale per Studi ed Esperienze di Architettura Navale, Via di Vallerano,139-00128 Roma, Italy

SUMMARY

An application of multidomain decomposition to the computation of the steady free surface flow past a ship hull is presented. Viscous effects are taken into account in the neighbourhood of solid walls and in the wake by the Reynolds averaged Navier–Stokes equations, whereas the assumption of irrotationality in the external flow allows a description by a potential model. Free surface boundary conditions have been implemented in a linearized form at the undisturbed waterplane. Suitable matching conditions are enforced at the interface between the viscous and the potential regions. The numerical results obtained for two merchant ship forms (the HSVA tanker and the Series 60 hull) are compared with experimental data available in the literature.

KEY WORDS: domain decomposition; free-surface; ship flow; viscous flow

1. INTRODUCTION

The main features of the flow around a ship hull are the existence of a fully three dimensional turbulent boundary layer over most of the hull, the possible generation of longitudinal vortex pairs at the bow and at the bilge, the presence of a complicated free surface wave pattern and its interaction with the boundary layer and the wake. The numerical simulation of this flow field is a challenging practical application for CFD but a difficult problem to deal with, because of the extremely large Reynolds numbers ($\sim 10^8$–10^9) at which actual ships operate, and because of the moving boundary at the air–water interface. The solution of the Navier–Stokes equations generally requires such a large amount of CPU time that numerical codes based on these equations become unfeasible for a customary usage in ship design. To overcome these difficulties, the decomposition suggested by Froude[1] has generally been used: gravity and viscosity are supposed to act separately and the mutual interaction of these effects is neglected. Potential flow models are used for the computation of the wave resistance R_w and the wave pattern, while viscous equations are solved ignoring the effects of waves, that is assuming a fixed (undisturbed) free surface regarded as a slip plane. Although the Froude decomposition allows a satisfactory prediction of both wave and viscous drag for slender hulls, mutual interaction of gravity and viscous forces may be important in the prediction of the hydrodynamic performances of full-form hulls, transom stern ships and twin-hull vessels. It is therefore a major problem in numerical prediction methods to take into account this influence.

The zonal approach concepts can be fruitfully exploited to save CPU time in the computation of the complete ship problem. Viscous effects may be considered only near the solid walls and in the wake, while the external flow field may be assumed to be inviscid. From the historical point of view, boundary layer methods were the first ones used to make the computation easier. These approaches were widely applied in aeronautical engineering from the late 1960s (for a general review see, for example, References 2 and 3), while their application to a simple naval problem (double-model flow,

CCC 0271–2091/95/090699–24

Received September 1994
Revised February 1995

i.e. the flow past the ship and its image with respect to the undisturbed water plane) is more recent,[4,5] and even more recent is the application to free surface viscous flows.[6] In classical boundary layer models, the viscous layer is assumed to be thin with respect to the local radius of curvature of the body surface. The equations of these models are parabolic: the influence of the downstream flow is neglected and the pressure is assumed to be constant through the boundary layer and equal to the external pressure. In the absence of separation, inviscid and boundary layer flow theories are usually applied with a coupled procedure (direct method) to take into account displacement effects. In the presence of separation, direct boundary layer methods cannot be used; an initial guess for the displacement thickness is assumed in the flow reversal zone, and it is iteratively adjusted to match the external pressure (inverse methods[7]).

The application of these methods to three dimensional ship flows may have a limited success when the thick boundary layer and the wake show a fully 3D nature, with large crossflow and strong longitudinal vortices, especially near the bow and the stern, where the curvature of the hull surface is large. Moreover this kind of approaches may give rise to some difficulties when dealing with full-form hulls and transom sterns or for ships advancing in drift motion. In all these cases the definition of the displacement thickness is not easy, especially when boundary layer separation occurs.

A method that describes the flow near the hull by the Navier–Stokes equations can be found in Reference 8, where the displacement thickness idea is retained only to define the boundary of the potential flow domain. With this approach, all the limits implied in the boundary layer model are overcome and, in fact, very good results can be found in the cited paper. Nevertheless, the difficulties regarding the definition of the displacement thickness in the cases mentioned above still remain. Moreover the regridding of the boundary of the potential flow field and the computation of the influence coefficient required at each iteration can be CPU time consuming.

The present method is not based on the concept of displacement thickness, but it assumes a fixed decomposition of the fluid domain, with a matching surface, on which appropriate conditions are imposed, located *a priori*. A panel method is used for the solution of the potential free surface flow, whereas the Reynolds averaged Navier–Stokes equations are discretized by a finite volume technique. The linearized model of Dawson[9] has been used in the external flow, where the double model flow is chosen as basis flow for the linearization of the free surface boundary conditions. In the internal region these conditions are linearized in the sense that they are imposed on the undisturbed water plane, while the nonlinear relation between pressure and velocity is retained. The choice of a linear potential model is dictated by the need of CPU time saving; at the same time, the Dawson model was preferred among the others because it allows a satisfactory prediction of the free surface pattern.[10]

The matching conditions to be used with linearized free surface flows deserve particular attention. In fact, the splitting of the external flow in a double model flow plus a perturbation term must be taken into account when forcing the matching conditions: the double model potential has to match the viscous double model flow, while the perturbation potential must be related to the difference between the free surface and the double model viscous flow. Therefore, a double model iterative computation is initially required to define the basis flow, then the free surface flow can be computed for each Froude number.

The present work can be seen as a sequel of References 11–13, where the authors started the analysis of domain decomposition techniques for free surface flows. In the previous work the global domain was divided into two non-overlapping zones; we have now analysed a domain decomposition with overlapping that seems to show better convergence properties in the iterative algorithm and a more regular transition of the solution from the inner to the outer domain at the matching boundaries.

In the following sections, the viscous and inviscid solvers are described and the coupling procedure is analysed. Some numerical examples are discussed and compared with experimental data.

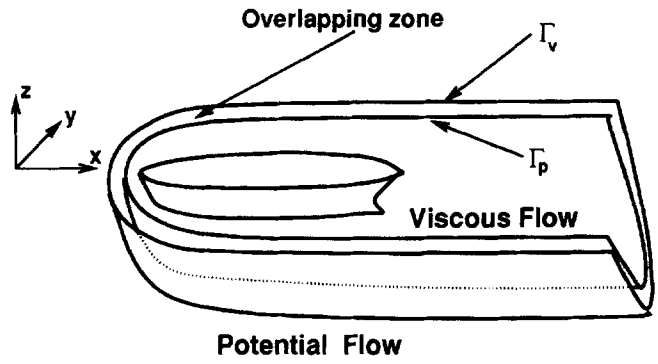

Figure 1. Computational sub-domains and overlapping zone

2. MATHEMATICAL MODEL

In the following, we consider the steady flow past a ship hull $\mathscr{B}$ floating in an incompressible viscous fluid. The flow domain is bounded by the free surface $\mathscr{S}$, by the hull surface and extends to infinity. We assume a body-fixed reference frame with the x-axis aligned with the ship and oriented from the bow to the stern; the z-axis is positive upwards (Figure 1).

The fluid is assumed inviscid and the flow irrotational in the subdomain $\mathscr{D}_p$ of the flow domain $\mathscr{D}$ that lies outside the surface Γ_p, whereas viscosity effects are taken into account in the inner region $\mathscr{D}_v$ bounded by Γ_v and the hull surface (see Figure 1). The two subdomains intersect over the region between Γ_p and Γ_v.

The variables have been non-dimensionalized by the ship length L and the free stream velocity U. Two parameters characterize the flow: the Froude number $Fr = U/(gL)^{\frac{1}{2}}$ and the Reynolds number $Re = UL\rho/\mu$, where ρ is the fluid density, g the acceleration of gravity and μ the dynamic viscosity.

2.1. *The outer region*

The fluid velocity $\mathbf{u} = (u, v, w)$ can be written as the gradient of a scalar function Φ:

$$\mathbf{u}(x, y, z) = \nabla\Phi(x, y, z). \tag{1}$$

The potential Φ is harmonic in $\mathscr{D}_p$. The boundary conditions to be enforced are:

(i) Neumann boundary conditions on Γ_p, i.e.

$$\frac{\partial\Phi}{\partial n} = \mathscr{W}_n \quad \text{on } \Gamma_p, \tag{2}$$

where $\mathscr{W}_n$ is the matching condition to be specified later on.

(ii) At the free surface $\mathscr{S}: z = \mathscr{H}(x, y)$ the pressure must be equal to the atmospheric pressure and therefore constant. From the Bernoulli theorem we have the dynamic condition:

$$\mathscr{H}(x, y,) = \frac{Fr^2}{2}\{1 - |\nabla\Phi[x, y, \mathscr{H}(x, y,)]|^2\}, \tag{3}$$

where surface tension has been neglected. The tangency of the flow to the unknown free surface gives the kinematic boundary condition

$$\frac{\partial\mathscr{H}}{\partial x}\frac{\partial\Phi}{\partial x} + \frac{\partial\mathscr{H}}{\partial y}\frac{\partial\Phi}{\partial y} = \frac{\partial\Phi}{\partial z}. \tag{4}$$

For computational purposes, the potential Φ is split into the double model term φ and the perturbation term $\tilde{\varphi}$:

$$\Phi(x, y, z) = \varphi(x, y, z) + \tilde{\varphi}(x, y, z). \tag{5}$$

The double model potential φ is used as basis flow for the linearization. It describes the flow past the body $\mathscr{B}$ and its image $\mathscr{B}'$, symmetric with respect to the (x, y)-plane (i.e. $\varphi_z(x, y, 0) \equiv 0$). The double model potential satisfies the matching condition

$$\frac{\partial \varphi}{\partial n} = \mathscr{V}_n \quad \text{on } \Gamma_p. \tag{6}$$

The perturbation term describes the departure of the flow from the double model solution. It satisfies

$$\frac{\partial \tilde{\varphi}}{\partial n} = \tilde{\mathscr{V}}_n \quad \text{on } \Gamma_p, \tag{7}$$

where $\tilde{\mathscr{V}}_n$ is such that

$$\frac{\partial \varphi}{\partial n} + \frac{\partial \tilde{\varphi}}{\partial n} = \frac{\partial \Phi}{\partial n} = \mathscr{V}_n + \tilde{\mathscr{V}}_n = \mathscr{W}_n \quad \text{on } \Gamma_p \tag{8}$$

$\mathscr{V}_n$ will be specified with $\mathscr{W}_n$ in Section 5. Then, the free surface boundary conditions are linearized following Dawson[9]: the squares of the derivatives of $\tilde{\varphi}$ are neglected and the kinematic and dynamic boundary conditions are merged to yield the unified boundary condition

$$\varphi_l^2 \tilde{\varphi}_{ll} + 2\varphi_l \varphi_{ll} \tilde{\varphi}_l + \frac{1}{Fr^2} \tilde{\varphi}_z = -\varphi_l^2 \varphi_{ll}, \tag{9}$$

where all terms in φ are known from the double model solution, and l is the curvilinear abscissa defined along the double model streamlines on $z = 0$.

Finally, the asymptotic behaviour of the wave potential $\tilde{\varphi}(x, y, z)$ at infinity must be specified. Waves should never propagate upstream; this gives the radiation condition:

$$\lim_{x \to -\infty} |\nabla \tilde{\varphi}(x, y, z)| = 0 \tag{10}$$

for every fixed (y, z) in $\mathscr{D}_p$.

2.2. *The inner region*

The Reynolds averaged Navier–Stokes equations describe the flow in the inner region $\mathscr{D}_v$. The velocity field is divergence free

$$\nabla \cdot \mathbf{u} = 0 \quad \text{in } \mathscr{D}_v \tag{11}$$

and the momentum equation has to be satisfied

$$\mathbf{u} \cdot \nabla \mathbf{u} + \nabla P = \nabla \cdot \boldsymbol{\tau} \quad \text{in } \mathscr{D}_v. \tag{12}$$

In the previous equation P is the 'total' pressure, i.e. the sum of the pressure term and the gravity term

$$\nabla P = \frac{\nabla p}{\rho} + \frac{\mathbf{k}}{Fr^2} = \nabla \left[\frac{p}{\rho} + \frac{z}{Fr^2} \right], \tag{13}$$

$\mathbf{k}$ being the unit vector aligned with the z-axis. $\boldsymbol{\tau}$ is the stress tensor, including the turbulent stresses

$$\boldsymbol{\tau} = \left(\frac{1}{Re} + \nu_T \right) [(\nabla u) + (\nabla u)^{\mathrm{T}}], \tag{14}$$

ν_T being the kinematic eddy viscosity. In the present work the Baldwin–Lomax turbulence model[14] has been used.

Apart from the surface Γ_v at which the potential and the viscous solutions are matched (this topic will be discussed later on), the boundary conditions to be imposed are the standard ones for Navier–Stokes computations. At the solid wall no slip conditions are enforced, i.e. velocity is set to zero at the boundary (no conditions are required for the pressure). On the free surface, the boundary conditions to be satisfied are the following:

(*a*) the kinematic boundary condition

$$u\frac{\partial \mathscr{H}}{\partial x} + v\frac{\partial \mathscr{H}}{\partial y} = w; \tag{15}$$

(*b*) the dynamic boundary condition (constant pressure on $\mathscr{S}_v$)

$$P = \mathscr{H}/Fr^2; \tag{16}$$

(*c*) zero tangential stresses

$$\tau_{xz} = 0, \qquad \tau_{yz} = 0. \tag{17}$$

3. NUMERICAL MODEL

In the numerical solution of the mathematical model depicted in Section 2 we can exploit the symmetry of the problem about the (x, z)-plane (the study is limited to ships advancing in rectilinear motion with no drift), and therefore only half of both subdomains is discretized. Symmetry conditions are imposed at $y = 0$ for the viscous flow

$$\left.\frac{\partial u}{\partial y}\right|_{y=0} = 0, \qquad \left.\frac{\partial w}{\partial y}\right|_{y=0} = 0, \qquad v\Big|_{y=0} = 0, \qquad \left.\frac{\partial p}{\partial y}\right|_{y=0} = 0, \tag{18}$$

while the method of images is used to reduce the number of unknowns in the potential problem.

3.1. Potential solver

The solution of the mathematical model described in Section 2.1 can be obtained by a panel method. In the following, $\bar{\Gamma}_p$ and $\bar{\mathscr{S}}_p$ are the discretized portions of the boundaries Γ_p and $\mathscr{S}_p$ respectively. The double model term φ can be represented by a simple layer potential distributed on $\bar{\Gamma}_p$

$$\varphi(P) = \int_{\bar{\Gamma}_p} \sigma(Q)\left[\frac{1}{|P-Q|} + \frac{1}{|P-Q'|}\right] \mathrm{d}S_Q, \tag{19}$$

where $P = (x, y, z) \in \mathscr{D}_p$, $Q = (x_Q, y_Q, z_Q) \in \bar{\Gamma}_p$, $Q' = (x_Q, y_Q, -z_Q)$.

If (19) is introduced in (6) we obtain the integral equation to be solved numerically. To this end, the boundary $\bar{\Gamma}_p$ of $\mathscr{D}_p$ is discretized into N_Γ plane quadrilateral elements L_k, $k = 1, \ldots, N_\Gamma$, and the simple layer intensity $\sigma(Q)$ is assumed piecewise constant. The discrete form of the integral equation (6) for $\sigma(Q)$ reads

$$\sum_{\substack{k=N_S+1 \\ k\neq i}}^{N} \sigma_k \left\{\frac{\partial}{\partial n_P}\int_{L_k} [|P-Q|^{-1} + |P-Q'|^{-1}]\,\mathrm{d}S_Q\right\}_{P=P_i} - 2\pi\sigma_i = \mathscr{V}_n(P_i) \tag{20}$$

for $i = N_S + 1, \ldots, N$, Equation (20) can be rewritten in the following form:

$$\sum_{\substack{k=N_S+1 \\ k\neq i}}^{N} \sigma_k[\mathbf{n}(P_i)\cdot(\mathbf{V}_k(P_i)+\mathbf{V}'_k(P_i))] - 2\pi\sigma_i = \mathscr{V}_n(P_i), \tag{21}$$

where $\mathbf{V}_k \equiv (V_{k_x}, V_{k_y}, V_{k_z})$ and $\mathbf{V}'_k \equiv (V'_{k_x}, V'_{k_y}, V'_{k_z})$ are

$$\mathbf{V}_k(P) = \int_{L_k} \frac{P-Q^*}{|P-Q|^3}\,\mathrm{d}S_Q, \tag{22}$$

$$\mathbf{V}'_k(P) = \int_{L_k} \frac{P-Q^*}{|P-Q'|^3}\,\mathrm{d}S_Q. \tag{23}$$

The resulting system of N_Γ linear equations in the N_Γ unknowns σ_k is solved with the LU factorization.

Similarly, the perturbation term $\tilde{\varphi}$ can be represented by a simple layer potential on $\bar{\Gamma}_p$ and the part $\bar{\mathscr{S}}_p$ of the free surface included in the boundary of $\mathscr{D}_p$:

$$\tilde{\varphi}(P) = \int_{\bar{\Gamma}_p \cup \bar{\mathscr{S}}_p} \tilde{\sigma}(Q)\frac{1}{|P-Q|}\,\mathrm{d}S_Q, \tag{24}$$

where $Q = (x_Q, y_Q, z_Q) \in \bar{\Gamma}_p \cup \bar{\mathscr{S}}_p$. As for the double model problem, (24) is introduced in (7) and (9) to obtain the integral equations to be solved numerically. We discretize $\bar{\Gamma}_p \cup \bar{\mathscr{S}}_p$ into $N = N_S + N_\Gamma$ plane quadrilateral elements L_k, $k = 1, \ldots, N$. N_Γ denotes the number of panels located on $\bar{\Gamma}_p$ and N_S the number of those located on the average free surface $\bar{\mathscr{S}}_p$. The discrete forms of equation (7) is

$$\sum_{\substack{k=1 \\ k\neq i}}^{N} \tilde{\sigma}_k[\mathbf{n}(P_i)\cdot\mathbf{V}_k(P_i)] - 2\pi\tilde{\sigma}_i = \tilde{\mathscr{V}}_i(P_i) \quad (i = N_S+1, \ldots, N), \tag{25}$$

while, for equation (9),

$$[\varphi_l(P_i)]^2 \sum_{k=1}^{N} \tilde{\sigma}_k \mathbf{l}(P_i)\cdot\nabla[\mathbf{l}(P_i)\cdot\mathbf{V}_k(P_i)] + 2\varphi_l(P_i)\varphi_{ll}(P_i)\sum_{k=1}^{N}\tilde{\sigma}_k\mathbf{l}(P_i)\cdot\mathbf{V}_k(P_i)$$

$$+\frac{1}{Fr^2}\left[\sum_{\substack{k=1 \\ k\neq i}}^{N}\tilde{\sigma}_k V_{k_z}(P_i) + 2\pi\tilde{\sigma}_i\right] = -[\varphi_l(P_i)]^2\varphi_{ll}(P_i) \quad (i = 1, \ldots, N_S), \tag{26}$$

where $\mathbf{l}(P_i)$ is the unit vector tangent to the double model streamlines on $z = 0$, and

$$\varphi_l(P_i) = [\varphi_x^2(P_i) + \varphi_y^2(P_i)]^{\frac{1}{2}}.$$

The derivatives of $\mathbf{V}_k(P)$ are approximated with second-order upwind finite differences along the co-ordinate lines. The upwind bias on each co-ordinate direction is determined by the corresponding double model velocity component. The radiation condition (10) is enforced in the following discrete form:

$$\sum_{\substack{k=1 \\ k\neq j}}^{N_j} \tilde{\sigma}_k V_{k_z}(P_j) - 2\pi\tilde{\sigma}_j = 0, \tag{27}$$

where $j = 1, \ldots, N_j$ is the index set corresponding to all panels whose control points $P_j \equiv (x_j, y_j, 0)$ are such that $x_j < x_r$ (see Figure 2), where $x = x_r$ is a plane that lies halfway the beginning of the potential domain and the bow of the ship. These equations replace the N_j equations (26) corresponding to the control points P_j.

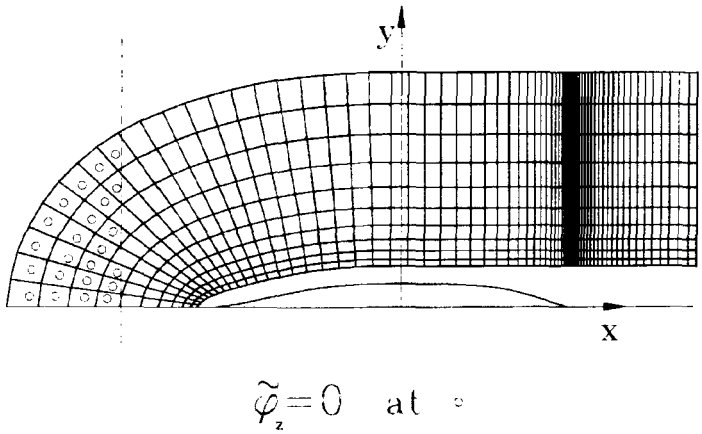

Figure 2. Control points where the radiation condition is enforced

The linear system (25)–(27) of N equations in the N unknowns $\tilde{\varphi}_k$ is solved, as in the double model problem, by LU factorization.

The reader is referred to Reference 15 for a rigorous and extensive discussion of the topics illustrated in this section.

3.2. *Navier–Stokes solver*

A well established implicit scheme developed in Reference 16 has been used for the numerical solution of the problem described in Section 2.2.

A pseudo-transient formulation due to Chorin[17] is used to solve the steady state incompressible Reynolds averaged Navier–Stokes equations. In this scheme the continuity equation is replaced by a transient counterpart

$$\frac{\partial p}{\partial t} + \beta \nabla \cdot \mathbf{u} = 0, \tag{28}$$

where β is the pseudo-compressibility factor. The resulting system of conservation laws is

$$\frac{\partial \mathbf{q}}{\partial t} + \frac{\partial \mathbf{F}^1}{\partial x} + \frac{\partial \mathbf{F}^2}{\partial y} + \frac{\partial \mathbf{F}^3}{\partial z} = \frac{\partial \mathbf{q}}{\partial t} + \frac{\partial \mathbf{F}^i}{\partial x_i} = 0, \tag{29}$$

where

$$\mathbf{q} = \begin{pmatrix} p \\ u \\ v \\ w \end{pmatrix}, \qquad \mathbf{F}^1 = \begin{pmatrix} \beta u \\ u^2 + p - \tau_{xx} \\ uv - \tau_{yx} \\ uw - \tau_{zx} \end{pmatrix},$$

$$\mathbf{F}^2 = \begin{pmatrix} \beta v \\ vu - \tau_{xy} \\ v^2 + p - \tau_{yy} \\ vw - \tau_{zy} \end{pmatrix}, \qquad \mathbf{F}^3 = \begin{pmatrix} \beta w \\ wu - \tau_{xz} \\ wv - \tau_{yz} \\ w^2 + p - \tau_{zz} \end{pmatrix}, \tag{30}$$

If $(\xi, \eta, \zeta) \equiv (\xi_1, \xi_2, \xi_3)$ is a curvilinear coordinate system, and we set $(x, y, z) \equiv (x_1, x_2, x_3)$, equation (29) can be recast in the form

$$\frac{\partial \mathbf{q}}{\partial t} + \frac{1}{J} \frac{\partial}{\partial \xi_k} [J \xi_{k,i} \mathbf{F}^i] = 0, \tag{31}$$

where the summation convention on repeated indices is adopted from here on for sake of conciseness, J is the Jacobian and $(\cdot)_i \equiv \partial(\cdot)/\partial x_i$.

A finite volume technique is used to discretize equation (31). The inner region $\mathscr{D}_v$ is divided in hexahedra V_{ijk}. The application of the Gauss theorem in the control volume V_{ijk} yields

$$\frac{\partial \mathbf{q}_{ijk}}{\partial t} + \mathbf{R}(\mathbf{q})_{ijk} = 0, \tag{32}$$

with

$$\mathbf{R}(\mathbf{q})_{ijk} = \frac{1}{V_{ijk}} \iint_{S_{ijk}} \mathscr{F} \cdot \mathbf{n} \, dS = 0, \tag{33}$$

where S_{ijk} is the boundary of V_{ijk}, $\mathbf{n} = (n_x, n_y, n_z)$ is the outer normal to S_{ijk} and $\mathscr{F} = (\mathbf{F}^1, \mathbf{F}^2, \mathbf{F}^3)$. In the numerical approximation the values of $\mathscr{F}$ on the faces of the cell V_{ijk} are needed for the discretization of equation (32): a simple averaging of neighbouring points is used to obtain velocity and pressure, while the stress tensor is evaluated by centred differencing.

The time marching procedure follows Beam and Warming[18]

$$\frac{\mathbf{q}^{n+1} - \mathbf{q}^n}{\Delta t} = (1 - \theta) \frac{\partial \mathbf{q}}{\partial t}\bigg|^n + \theta \frac{\partial \mathbf{q}}{\partial t}\bigg|^{n+1} = -(1 - \theta)\mathbf{R}(\mathbf{q}^n) - \theta \mathbf{R}(\mathbf{q}^{n+1}) \tag{34}$$

where $0 \leqslant \theta \leqslant 1$. Using a Taylor expansion, equation (34) can be written in 'delta' form

$$\left[\delta \mathbf{q} + \frac{\theta \Delta t}{J} \frac{\partial}{\partial \xi_l} \left(J \xi_{l,m} \mathbf{A}^m \delta \mathbf{q} + J \xi_{l,m} \mathbf{B}^{m,r} \frac{\partial \delta \mathbf{q}}{\partial \xi_r} \right) \right]^n = -\Delta t \mathbf{R}(\mathbf{q}^n), \tag{35}$$

where $\delta^n = \mathbf{q}^{n+1} - \mathbf{q}^n$, $\mathbf{A}^m$ and $\mathbf{B}^{m,r}$ are the jacobians of $\mathbf{F}^m$:

$$\mathbf{A}^m = \frac{\partial \mathbf{F}^m}{\partial \mathbf{q}}, \quad \mathbf{B}^{m,r} = \frac{\partial \mathbf{F}^m}{\partial \mathbf{q}_{\xi_r}}. \tag{36}$$

A direct solution of the system of algebraic equations (35) would be too expensive, thus an approximate factorization technique is used to reduce it to the solution of three simpler problems, with block tridiagonal coefficient matrix:

$$[\mathbf{I} + \theta \Delta t (\mathscr{A}^1 + \mathscr{A}^2 + \mathscr{A}^3)] \delta \mathbf{q}^n \simeq (\mathbf{I} + \theta \Delta t \mathscr{A}^1)(\mathbf{I} + \theta \Delta t \mathscr{A}^2)(\mathbf{I} + \theta \Delta t \mathscr{A}^3) \delta \mathbf{q}^n, \tag{37}$$

with accuracy $O(\Delta t)$. The operator $\mathscr{A}$ introduced in the factorization is defined as

$$\mathscr{A}^l = \frac{1}{J} \frac{\partial}{\partial \xi_l} \left(J \xi_{l,m} \mathbf{A}^m + J \xi_{l,m} \mathbf{B}^{m,l} \frac{\partial}{\partial \xi_l} \right), \tag{38}$$

with no summation on l. It can be noticed that all the second-order mixed derivative in $\delta \mathbf{q}$ were discarded in the implicit part of the system to maintain the tridiagonal structure. This approximation, however, does not affect the steady state solution.

To ensure the numerical stability of the scheme, a fourth order artificial dissipation term is added to both sides of (37). Thus the flux at the interface $\xi_1|_{i+\frac{1}{2},j,k}$ is modified according to

$$\tilde{\mathscr{F}} \cdot \mathbf{n}|_{i+\frac{1}{2},j,k} = \mathscr{F} \cdot \mathbf{n}|_{i+\frac{1}{2},j,k} + \varepsilon_e \bar{V} (\mathbf{q}_{i+2,j,k} - 3\mathbf{q}_{i+1,j,k} + 3\mathbf{q}_{i,j,k} - \mathbf{q}_{i-1,j,k}), \tag{39}$$

ε_e being a parameter $O(1)$ and $\bar{V}$ the average volume of the two neighbouring cells. A second-order term is added to each tridiagonal operator in the left-hand side

$$\tilde{\mathscr{A}}^l = \frac{1}{J}\frac{\partial}{\partial \xi_l}\left(J\xi_{l,m}\mathbf{A}^m + J\xi_{l,m}\mathbf{B}^{m,l}\frac{\partial}{\partial \xi_l} - \varepsilon_i \bar{V}\frac{\partial}{\partial \xi_l}\right), \tag{40}$$

where ε_i is again $O(1)$.

The final form of the system of equations is, then

$$(\mathbf{I} + \theta\Delta t\tilde{\mathscr{A}}^1)(\mathbf{I} + \theta\Delta t\tilde{\mathscr{A}}^2)(\mathbf{I} + \theta\Delta t\tilde{\mathscr{A}}^3)\delta\mathbf{q}^n = -\Delta t\tilde{\mathbf{R}}(\mathbf{q}^n), \tag{41}$$

where $\tilde{\mathbf{R}}(\mathbf{q}^n)$ includes the artificial dissipation terms.

It can be shown that the steady state solution is second-order accurate and that the above scheme is unconditionally stable in the linear case if $\theta \geqslant 0{\cdot}5$ and $\varepsilon_i \geqslant 2\varepsilon_e$. The reader is referred to References 16 and 18 for a detailed discussion.

In the implementation of the numerical code, all the metric terms in the above relations were computed in a finite volume fashion, i.e. the Jacobian J_{ijk} was set equal to the volume cell V_{ijk} and the terms like $J\xi_i$ at the cell interfaces $\xi = \text{const.}$ are computed, for instance, as

$$\begin{aligned} J\xi_x|_{i+\frac{1}{2},j,k} &= n_x \Delta S_{i+\frac{1}{2},j,k}, \\ J\xi_y|_{i+\frac{1}{2},j,k} &= n_y \Delta S_{i+\frac{1}{2},j,k}, \\ J\xi_z|_{i+\frac{1}{2},j,k} &= n_z \Delta S_{i+\frac{1}{2},j,k}, \end{aligned} \tag{42}$$

where (n_x, n_y, n_z) is the outer normal to the interface and $\Delta S_{i+\frac{1}{2},j,k}$ is the area of the interface between $V_{i,j,k}$ and $V_{i+1,j,k}$. A speedup in the computation can be achieved if a local time step is used

$$\Delta t_{ijk} = CJ_{ijk}^{\frac{1}{3}} \tag{43}$$

with C a stability parameter.

The boundary conditions are enforced as follows:

Solid wall. At the cell interface of the hull surface $\mathbf{u}$ is set to zero. The normal gradient of the velocity, needed for the computation of the stress at the boundary, is computed with a first-order one-side difference, while the pressure is simply extrapolated from the cell centre adjacent to the wall.

Symmetry plane. The normal velocity, the normal gradient of the other velocity components and the normal gradient of the pressure are set to zero.

Outflow. The flow is supposed to be completely developed in this region and therefore both the pressure and the velocity vector are extrapolated (null gradient) from internal values.

Free surface. The wave elevation $\mathscr{H}$ is updated at each iteration by means of the unsteady kinematic boundary condition

$$\frac{\partial \mathscr{H}}{\partial t} + u\frac{\partial \mathscr{H}}{\partial x} + v\frac{\partial \mathscr{H}}{\partial y} = w, \tag{44}$$

which is discretized with a finite difference scheme

$$\mathscr{H}_{ij}^{n+1} = \mathscr{H}_{ij}^{n} - \Delta t\left[(u\xi_x + v\xi_y)_{ij}\left(\frac{\partial \mathscr{H}}{\partial \xi}\right)_{ij} (u\eta_x + v\eta_y)_{ij}\left(\frac{\partial \mathscr{H}}{\partial \eta}\right)_{ij}\right]. \tag{45}$$

The spatial derivatives of $\mathscr{H}$ in (45) are computed with second order upwind differences.

Once $\mathscr{H}$ is known, the total pressure at the free surface is computed from (16). The velocity components are simply extrapolated from the values at the cell centre below the waterplane. Condition

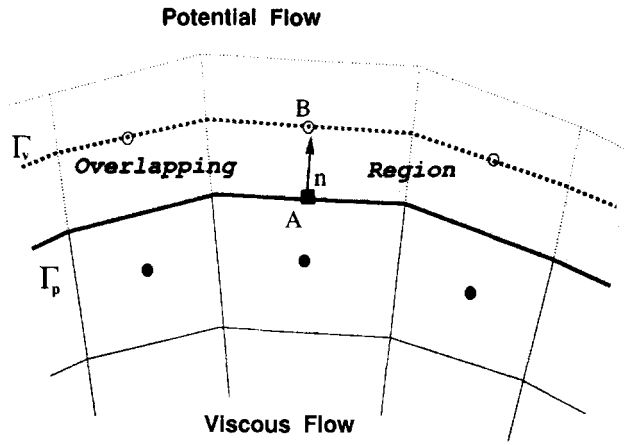

Figure 3. Location of the exchanged variables at the matching interfaces

(17) has not been used, because the dimension of the cells near the free surface does not allow the resolution of the boundary layer at the water–air interface, which is extremely thin, being $O(Fr/Re^{\frac{1}{2}})$.

Applications of this scheme to double model ship flow calculations can be found, for instance, in Reference 19 or 20.

4. MATCHING ALGORITHM

The numerical algorithm used to couple the inner and the outer solution is the most important step of the whole procedure. The choice of the exchanged variables and the location of the matching surface may deeply affect the convergence rate or even cause the failure of the algorithm. In the previous version of the method[11], a non-overlapping domain decomposition scheme was used. The values of the tangential component of the velocity and the pressure of the potential field at the matching surface were used as boundary conditions for the Navier–Stokes solver, while the normal component of the viscous solution was used as Neumann condition in the potential flow. With this kind of approach, the convergence was reached within round-off errors but the convergence rate was not very satisfactory and some relaxation factors had to be used when matching the solutions. Furthermore, non-smooth transition from the inner to the outer domain was observed.

In the present work, the algorithm has been changed. The flow domain is divided in two subdomains that overlap in a small region, as illustrated in Figures 1 and 3. These subdomains are bounded by Γ_p and Γ_v, which are the boundaries of the potential and viscous zones, respectively. The thickness of the overlapping region is equal to half the height of the outermost cells in the inner grid (Figure 3).

In the iterative coupling procedure, the solution computed in the first domain is used to feed the solution in the other domain with the boundary conditions, that is, in terms of the total potential Φ:

(i) from the potential solver we get the velocity vector at the grid point B on Γ_v (see Figure 3); these values are enforced as boundary conditions on the viscous flow

$$\mathbf{u}|_{\Gamma_v} = \nabla\Phi|_{\Gamma_v}; \tag{46}$$

(ii) the normal component of the velocity at the control point A on Γ_p (see Figure 3) is computed from the viscous flow solution. This value is then used as a Neumann condition for the potential problem (see equation (2))

$$\left.\frac{\partial\Phi}{\partial n}\right|_{\Gamma_p} = \mathscr{W}_n = \mathbf{u}\cdot\mathbf{n}|_{\Gamma_p}. \tag{47}$$

This new scheme improves the convergence rate, makes the relaxation factors useless and ensures a smooth transition across the matching surface.

As to the numerical implementation of matching conditions, we remind that for computational reasons the potential flow field is expressed as the sum of a double model potential φ and a perturbation potential $\tilde{\varphi}$. The multidomain solution has to be consistent with this decomposition, and therefore the solution must be obtained in two steps:

1. *Double Model Flow.* The solution is computed with the conditions

$$\begin{cases} w_0 = 0, \\ \dfrac{\partial u_0}{\partial z} = 0, \\ \dfrac{\partial v_0}{\partial z} = 0, \end{cases} \quad \text{on } \bar{\mathscr{S}}_v \qquad \text{and} \qquad \frac{\partial \varphi}{\partial z} = 0 \quad \text{on } \bar{\mathscr{S}}_p \tag{48}$$

on the waterplane $z = 0$, while the matching conditions on $\bar{\Gamma}_p$ and $\bar{\Gamma}_v$ are

$$\mathbf{u}_0\Big|_{\bar{\Gamma}_v} = \nabla\varphi\Big|_{\bar{\Gamma}_v}, \tag{49}$$

$$\frac{\partial \varphi}{\partial n}\bigg|_{\bar{\Gamma}_p} = \mathscr{V}_n = \mathbf{u}_o \cdot \mathbf{n}\Big|_{\bar{\Gamma}_p}, \tag{50}$$

where $\mathbf{u}_0$ is the velocity vector in the inner double model solution.

A uniform flow is assumed as initial condition.

2. *Free Surface Flow.* Once the double model solution is obtained with the desired accuracy, the free surface flow can be computed. The matching conditions to be enforced are slightly more complex than in the previous step. In fact, the potential $\tilde{\varphi}$ is a perturbation with respect to the double model flow and therefore it must be related to the difference between the free surface velocity field and the double model velocity field in the viscous domain. At the same time, the viscous solution, which is not split, must be related to the total potential. This yields the following matching conditions:

$$\mathbf{u}\Big|_{\bar{\Gamma}_v} = \tilde{\mathscr{V}}_n = \nabla(\varphi + \tilde{\varphi})\Big|_{\bar{\Gamma}_v}, \tag{51}$$

$$\frac{\partial \tilde{\varphi}}{\partial n}\bigg|_{\bar{\Gamma}_p} = \mathbf{u} \cdot \mathbf{n}\Big|_{\bar{\Gamma}_p} - \mathbf{u}_0 \cdot \mathbf{n}\Big|_{\bar{\Gamma}_p}. \tag{52}$$

The double model flow is chosen as initial guess, and therefore the onset matching condition (52) is $\partial\tilde{\varphi}/\partial n = 0$.

It is easy to verify that if (50) and (52) are summed, the global matching condition (47) is satisfied.

It is to be noticed that, in the practical implementation of the matching algorithm, we need to evaluate the pressure on $\bar{\Gamma}_v$. From the theoretical point of view, it is well known that the solution of the Navier–Stokes equations is completely determined by the boundary conditions (49) and (51) on $\bar{\Gamma}_v$ for the double model problem and for the free surface problem respectively. This means that no boundary condition must be enforced on the pressure field in the viscous subdomain at the matching boundary. On the other hand, its value is required for the computation of the fluxes normal to the cell interfaces on $\bar{\Gamma}_v$ and therefore it must be evaluated somehow. Numerical tests proved that first or second order extrapolations of the pressure from the inner of the domain $\mathscr{D}_v$ give rise to discontinuities and

oscillations of the solution at the matching boundary. Conversely, the evaluation of the pressure from the external field by means of the Bernoulli's theorem yield a smooth matching in the overlapping region. We stress that this is not to be regarded as a boundary condition; on the contrary, it is an estimate of the pressure, supported by the assumption of negligible viscous effects on $\bar{\Gamma}_v$.

The standard application of a multidomain decomposition technique would require the iterative coupling of the converged flow fields, each computed for assigned boundary conditions on the matching surfaces, as done in Reference 2.

The solution of the potential field for both the double model and the free surface problem is not very expensive to be computed, in that the problems are linear and therefore the coefficient matrix of the resulting system of equations can be computed and stored in factorized form at the beginning of the computation. In fact, the coupling procedure affects only the right-hand side of the system of equations in the unknown σ or $\tilde{\sigma}$, and therefore the solution can be calculated by back-substitution at each global step. We insist that in the potential free surface problem the coefficient matrix depends only on the double model solution that has already been computed at the previous stage, and therefore does not change while iterating, because the two problems have been solved separately, unlike that in Reference 21.

On the contrary, the steady solution of the Navier–Stokes equations is extremely time consuming, because we have to deal with a system of coupled non-linear equations, that must be solved iteratively. However, the convergence of the viscous solver to the steady state solution in the inner cycle of the iterative matching algorithm is not required, like in most nested iteration algorithms. In all the test cases we have performed, the Navier–Stokes solver was iterated for a fixed number N_{NS} of steps (typically $1 \leqslant N_{NS} \leqslant 100$) and the global algorithm never failed to converge. Nevertheless, the number of sub-iterations affects the global convergence rate. Some numerical experiments on this aspect will be shown in the next section.

5. NUMERICAL RESULTS

All the test cases presented in this section were computed with a workstation IBM RISC/6000 Mod. 560 equipped with 256 Megabyte of RAM with peak performances equal to 80 MFLOPS.

In numerical tests, three hull forms have been chosen. The Wigley hull was used in consistence tests. This hull, although of no practical interest, has often been used in both numerical and experimental test cases, because it has a simple analytical representation given by

$$\frac{y}{B} = \frac{1}{2}\left[1 - \left(\frac{2x}{L}\right)^2\right]\left[1 - \left(\frac{z}{d}\right)^2\right], \tag{53}$$

where $B/L = 0{\cdot}1$ and $d/L = 1/16$. L, B and d are the length, the breadth and the draft of the hull respectively. Two merchant ship forms, for which model basin experimental data or wind tunnel measurements are available, have been considered for the validation of the algorithm. The first one is the HSVA tanker, the geometry of which is reported in Figure 4. For this hull very detailed experimental measurements, carried out in the wind tunnel at University of Hamburg,[22] are available in terms of both pressure and velocity field for the double model flow. The second one is another typical test case hull, the Series 60 with $C_b = 0{\cdot}6$, where C_b is the block coefficient, defined as the ratio of the volume of water displaced by the ship to the product of the ship's length, breadth and draft (Figure 5). Detailed experimental data, measured at the IIHR (University of Iowa), are available for this hull for several free surface flows, with Froude number equal to 0·160, 0·250, 0·300 and 0·316.

The meshes used in the numerical tests are summarized in Table I, where $N_i \times N_j \times N_k$ in the inner domain means N_i cells in streamwise direction, N_j cells in normal direction and N_k cells in girthwise direction, while $N_{i_{\Gamma_p}} \times N_{k_{\Gamma_p}}$ is the number of panels on $\bar{\Gamma}p$ in streamwise and girthwise direction

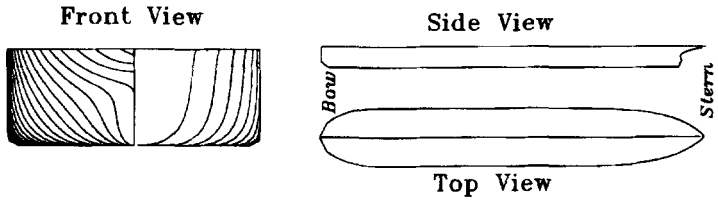

Figure 4. HSVA tanker: top view, side view and front view (afterbody cross sections on the left, forebody cross section on the right)

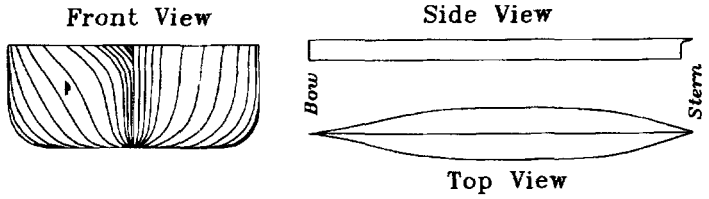

Figure 5. Series 60 hull: top view, side view and front view (afterbody cross sections on the left, forebody cross section on the right)

respectively. Finally, $N_{i_{Sp}} \times N_{k_{Sp}}$ is the number of panels on the waterplane in the potential subdomain $\mathcal{S}_p$, in streamwise and starboard direction, respectively.

In Figure 6 the coarse C-O grid used in the inner region for the computation of the double model flow past the HSVA tanker is shown. In this case we do not have the free surface grid. The computational mesh used for the Series 60 is shown in Figure 7, where the free surface C-type grid is shown together with the inner grid.

In all the computation performed, the cells in the viscous subdomain were clustered near the wall in order to have a satisfactory resolution of the strong boundary layer gradients of the tangential components of velocity. The normal size of the first cell near the wall was 10^{-5} in all the grids. Moreover, the cells were clustered near the bow and the stern, where significant gradients of both pressure and velocity are expected. The matching surface is $L/20$ far from the hull in both the HSVA tanker and the Series 60 in the fine grid computations, while it is placed at $L/10$ in the coarse HSVA grid.

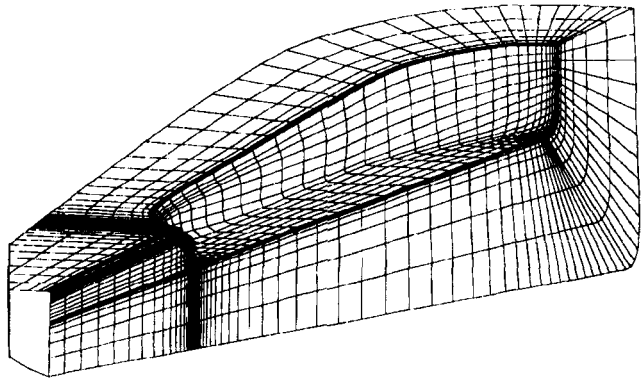

Figure 6. Sample grid around the HSVA tanker

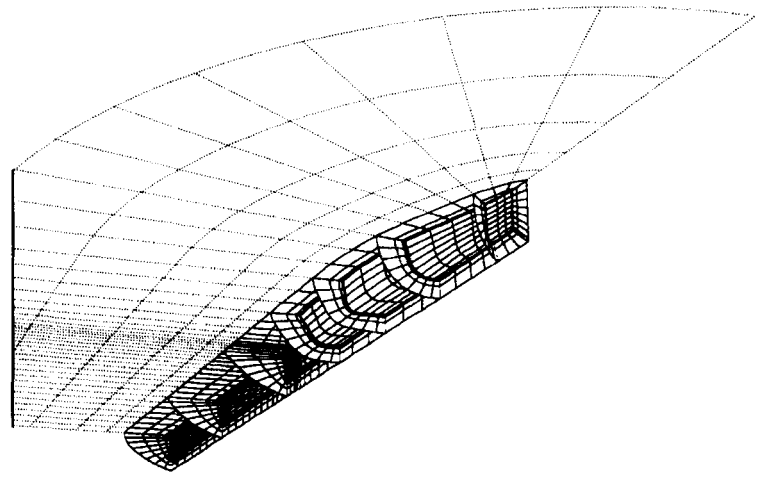

Figure 7. Sample grid used in the S60 computation. Dotted lines: free surface panel: solid lines: Navier–Stokes grid

5.1. Numerical behaviour of the algorithm

Before the comparison with the experimental data, some properties of the algorithm have been investigated.

5.1.1. Convergence properties. As an example of the consistency of matching conditions, we report the convergence history for the computation of the free surface flow past a Wigley hull advancing in calm water with $Fr = 0{\cdot}316$ and $Re = 4{\cdot}5 \times 10^6$.

The convergence history (L_2 norm of the divergence residual against the number of iterations of the Navier–Stokes solver), reported in Figure 8 for both the double model problem (the first part of the plot

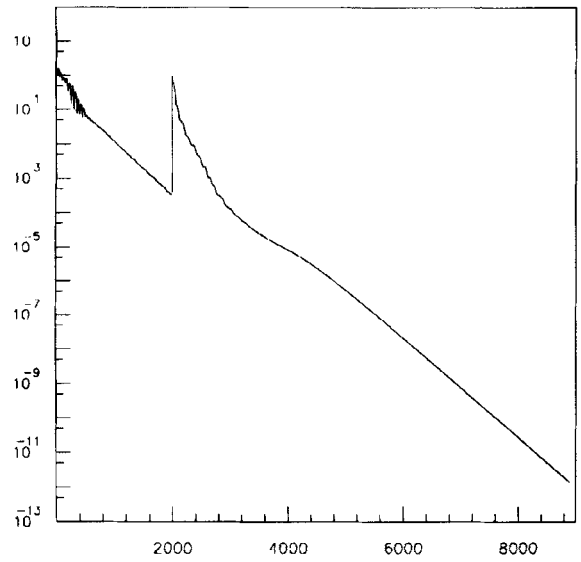

Figure 8. Convergence history of L_2 norm of the mass residual

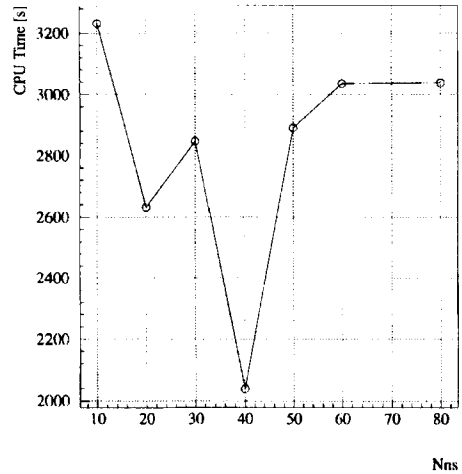

Figure 9. CPU times (in seconds) as function of the number of the Navier–Stokes iterations for each potential solver call

up to 2000 iterations) and the free surface problem, shows that the discrete problem can be solved with any desired accuracy, up to roundoff errors.

Next, the dependence of the convergence rate on the various parameter mentioned in the previous section is analysed. In Figure 9 the CPU time is reported as a function of N_{NS} (see the end of Section 4) for the computation of a free surface viscous flow with $Fr = 0{\cdot}316$ and $Re = 4 \times 10^6$ past the Series 60. The computation to which the picture refers was performed with the coarse grid mentioned in Table I. The CPU time reported in the figure (in seconds) is the time needed to low the initial L_2 norm of the residual of the divergence by a factor 10^{-5}. In the analysis reported, $N_{NS} = 40$ is the optimum value. However, a more extensive analysis is required to have a more reliable answer.

Figure 10 shows the CPU time (evaluated as in the previous case) as a function of the stability parameter C in (43). In this case, the CPU time reaches a minimum at $C = 0{\cdot}3$, beyond which it begins

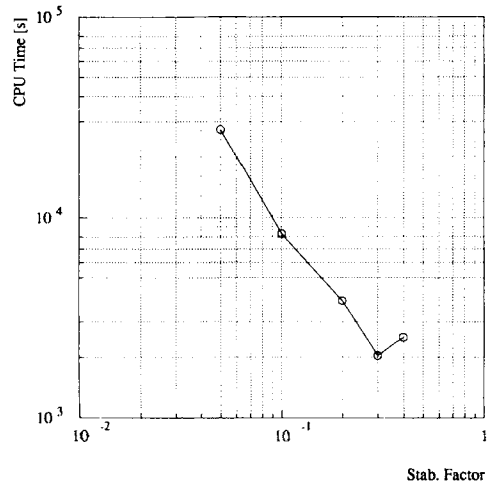

Figure 10. CPU time (in seconds) as function of the stability parameter

Table I

	coarse grid			fine grid		
	inner domain	outer domain		inner domain	outer domain	
		Γ_p	$\mathscr{S}_p$		Γ_p	$\mathscr{S}_p$
Wigley	65 × 15 × 15	65 × 15	65 × 15	—	—	—
HSVA	65 × 14 × 14	65 × 14	—	120 × 30 × 30	120 × 30	—
S60	80 × 10 × 14	80 × 14	80 × 10	120 × 15 × 24	120 × 24	120 × 15

to grow again. At $C = 0{\cdot}5$ the algorithm diverges. The previous comments on the reliability of this results still hold.

5.1.2. Grid dependence. The dependence of the numerical solution on the grid size was investigated for both the double model flow past the HSVA tanker and the free surface flow at $Fr = 0{\cdot}316$ for the Series 60. Figure 11 shows the comparison of the contour lines of the pressure on the hull, on the symmetry plane and on the water plane as computed with the coarse and fine grid for the flow past the HSVA tanker. The figure shows that the dependence of the numerical solution on the grid size is very weak. In Figure 12 the pressure contours obtained with the multidomain computation on the coarse grid and a full domain Navier–Stokes computation on a 80 × 30 × 24 grid are compared. The comparison of the performances of the two calculations is favourable to the multidomain algorithm and very encouraging: the required CPU times are 4 h with the zonal approach and 24 h in the full Navier–Stokes computation.

The same investigation was carried out for the free surface viscous flow past the S60 hull. The contour lines of the pressure computed with the coarse and the fine grids are compared in Figure 13 in the case $Fr = 0{\cdot}316$ and $Re = 4 \times 10^6$. Also in this case the agreement is rather satisfactory.

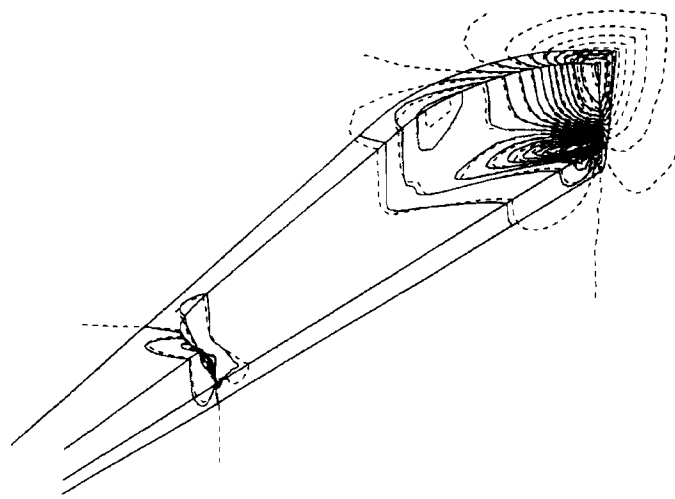

Figure 11. Pressure contour map: comparison between fine grid solution (solid line) and coarse grid solution (dashed line) for the HSVA tanker. Levels: $-0{\cdot}5$, $-0{\cdot}45$, ..., $0{\cdot}5$

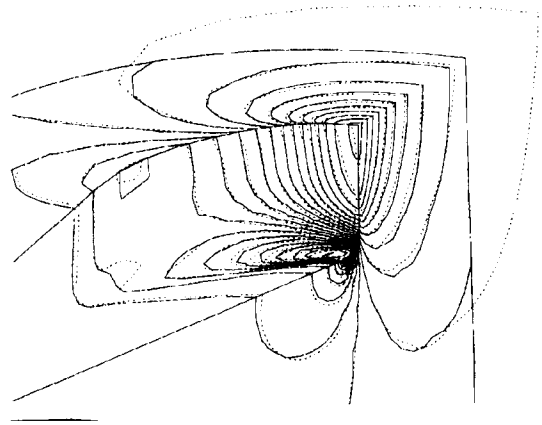

Figure 12. Pressure contour map: comparison between present method (solid line) and full viscous solution (dashed line) for the HSVA tanker. Levels: $-0{\cdot}5$, -0.45, ..., $0{\cdot}5$

5.1.3. Domain size dependence. The dependence of the numerical solution on the position on the surface $\bar{\Gamma}_p$ (and consequently on the size of the viscous subdomain) is reported in Figure 14, where the wave elevations on the hull and in the wake, obtained with two different positions of the matching surface, are shown. The solid line is the wave profile computed with the fine grid. The broken line is the wave profile computed with a grid which is identical to the previous one in the innermost part, while the five outermost arrays of cells were eliminated, i.e. the second grid has $120 \times 10 \times 24$ cells in the inner domain. The boundary of the potential field is discretized with the same number of panels as in the fine grid. In the computation with the fine grid, the matching surface is placed at 1/20 of the ship length aside from the hull, while in the second it is much closer to the ship (1/100). The two computation are in reasonable agreement, although in the second case the boundary of the viscous subdomain is very near to the region where viscous effects are important.

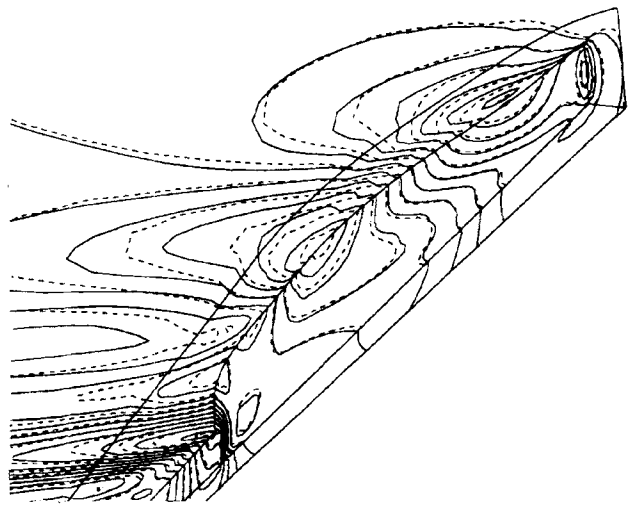

Figure 13. Pressure contour map: comparison between fine grid solution (solid line) and coarse grid solution (dashed line) for the free surface flow past the S60 hull $Fr = 0{\cdot}316$, $Re = 4 \times 10^6$. Levels: $-0{\cdot}12$, $-0{\cdot}10$, ..., $0{\cdot}12$

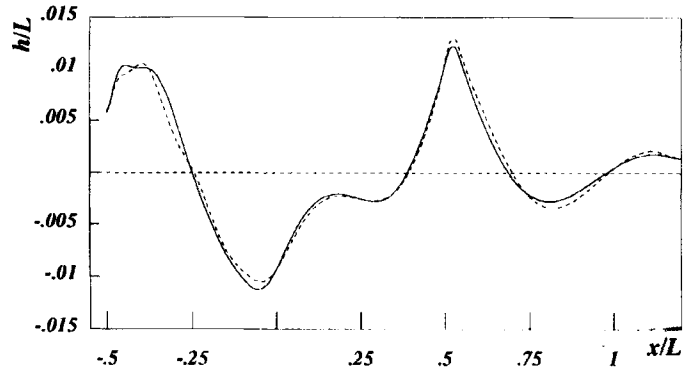

Figure 14. Wave profile on the hull: free surface flow past the S60 hull $Fr = 0{\cdot}316$, $Re = 4 \times 10^6$. Comparison between the solutions when the distance of $\bar{\Gamma}_p$ from the body is equal to L/20 (solid line) and L/100 (dashed line)

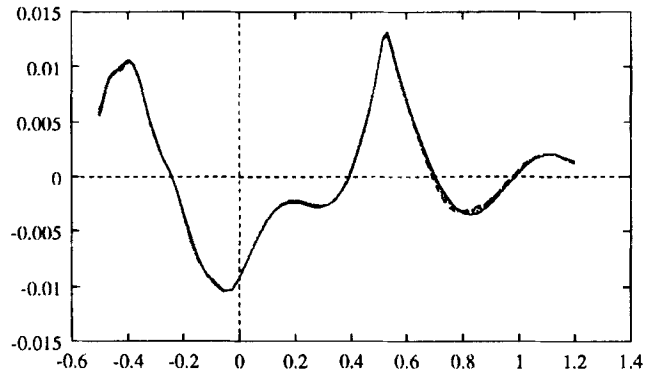

Figure 15. Wave profile on the hull: comparison of the solutions with $\varepsilon_e = 8; 4; 2; 1; 0{\cdot}5$ for the free surface flow past the S60 hull $Fr = 0{\cdot}316$, $Re = 4 \times 10^6$

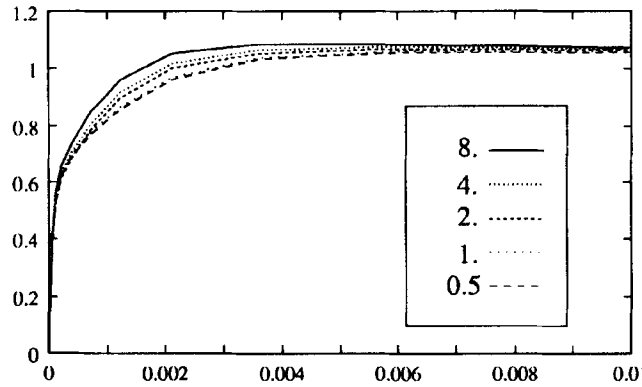

Figure 16. Boundary layer at midship on the waterplane: comparison of the solutions with $\varepsilon_e = 8; 4; 2; 1; 0{\cdot}5$ for the free surface flow past the S60 hull $Fr = 0{\cdot}316$, $Re = 4 \times 10^6$

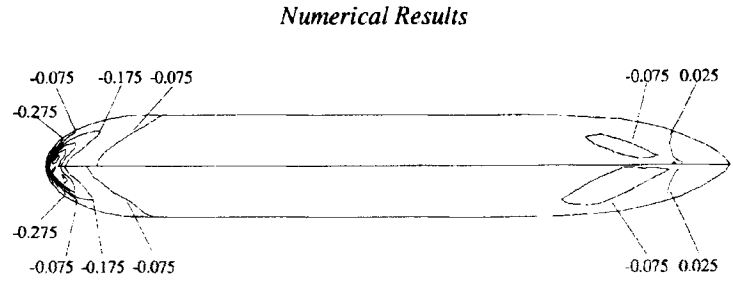

Figure 17. Pressure contour map: comparison between numerical results (top half) and experimental data[22] (bottom half) for the HSVA tanker. Levels: $-0{\cdot}5$, -0.475, ..., $0{\cdot}5$

Note that in the computations reported in Figure 11, for the double model flow past the HSVA tanker, the size of the inner domain is different for the coarse and fine grid, with $\bar{\Gamma}_p = L/10$ and $L/20$ far from the hull, respectively. The dependence on the domain size is moderate also for this test case.

5.1.4. Artificial viscosity dependence. Finally, the dependence of the numerical solution on artificial viscosity parameter ε_e (see (39)) was investigated. Five values of this parameter (8, 4, 2, 1, 0·5) were tested. In all the computations $\varepsilon_i = 2\varepsilon_e$. As it can be observed in Figure 15 and 16, the wave elevation is almost independent of the value of ε_e, while its influence on the velocity profiles in the boundary layer is more relevant. Figure 16 shows that the velocity profiles computed with $\varepsilon_e = 1$ and $\varepsilon_e = 0{\cdot}5$ are practically identical. However, ε_e cannot be further reduced, because spurious oscillations appear and the algorithm may fail to converge.

5.2. Comparisons with experiments

5.2.1. Double model flow past the HSVA tanker. In this section, the numerical results are compared with wind tunnel measurements for the double model flow past the HSVA tanker.[22]

In Figure 17 the computed pressure on the surface of the ship is compared with experimental data, showing a good agreement. The same cannot be said when comparing the velocity field near the stern (Figure 18). The computed solution fails to reproduce the main features of the axial velocity distribution in the wake; more in detail, the S-shaped contours observed experimentally are completely absent. This is a problem common to many numerical schemes, as it was noted in the Workshop held in Gothenburg in 1990.[23] This aspect was studied in great detail by Visonneau *et al.*[24], who analysed the dependence of the solution on the grid size and on the turbulence model. They proved that this incapability of numerical codes to feature this complex velocity field is mainly due to the turbulence models used in the simulation. However, the choice of a proper turbulence model is beyond the scope of the present study, and therefore the problem was no further analysed.

5.2.2. Free surface flow past the S60 hull ($C_b = 0{\cdot}6$). For the S60 hull, several non-zero Froude number computations have been performed.

The wave patterns are shown in Figures 19 and 20 for Froude numbers equal to 0·300 and 0·316 ($Re = 4{\cdot}5 \times 10^6$ in both cases). The computed solutions are compared with experimental measurements.[25] The comparison with the experimental measured wave profiles is satisfactory, in that the numerical simulation can predict the formation and interference of the stern and bow wave

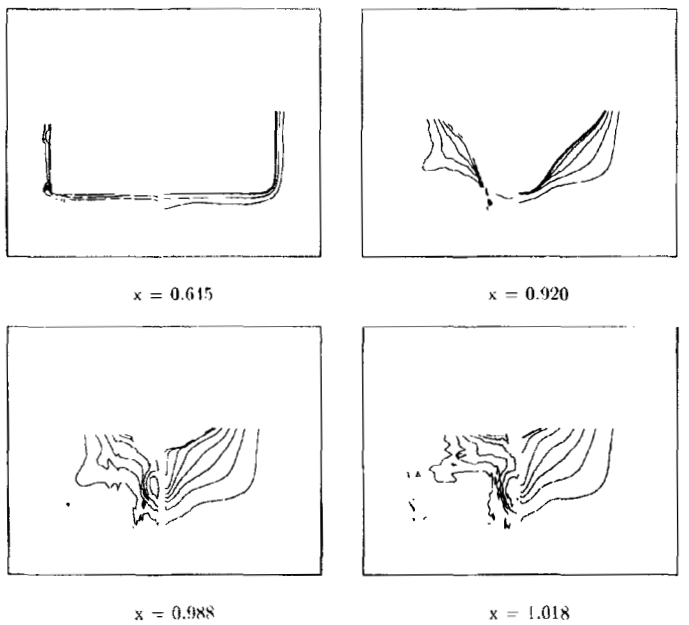

Figure 18. Axial velocity contour map: comparison between numerical results (right) and experimental data[22] (left) for the HSVA tanker at cross sections $x = 0{\cdot}645$, $0{\cdot}92$, $0{\cdot}988$, $1{\cdot}018$; levels: $0{\cdot}2$, $0{\cdot}3$, ..., $0{\cdot}9$

systems observed experimentally. It is worth noticing the good matching of the inner and the outer solutions at the surface $\bar{\Gamma}_p$.

The wave profiles along the hull are compared with experiments and with full potential calculations for four values of the Froude number ($0{\cdot}160$, $0{\cdot}250$, $0{\cdot}300$ and $0{\cdot}316$). Figure 21 shows that the prediction obtained with the multidomain technique fits the experiments better than the potential calculation at all the Froude numbers tested. Particularly relevant is the capability of the present method to capture the position of local maxima and minima of the wave profile and the good prediction of the bow crests at very low Froude numbers. This last aspect is likely to be due not only to

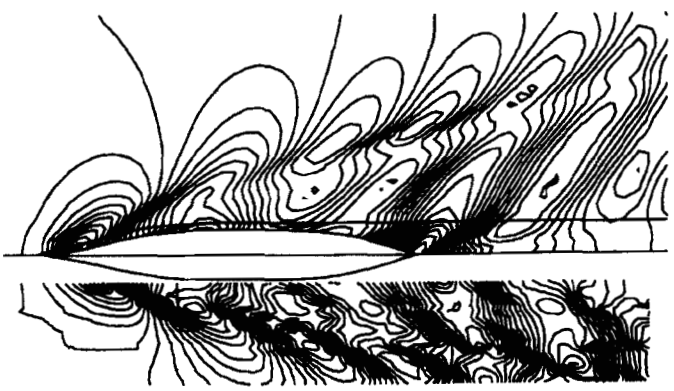

Figure 19. Free surface elevation: comparison between numerical results (top half) and experimental data[26] (bottom half) for the S60—$Fr = 0{\cdot}300$. Levels of $\mathscr{H}/Fr^2$: $-0{\cdot}1$, -0.09, ..., $0{\cdot}1$

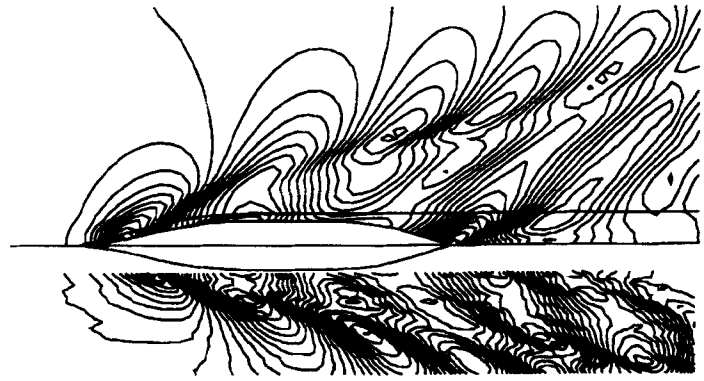

Figure 20. Free surface elevation: comparison between numerical results (top half) and experimental data[26] (bottom half) for the S60—$Fr = 0{\cdot}316$. Levels of $\mathscr{K}/Fr^2$: $-0{\cdot}1$, $-0{\cdot}09$, ..., $0{\cdot}1$

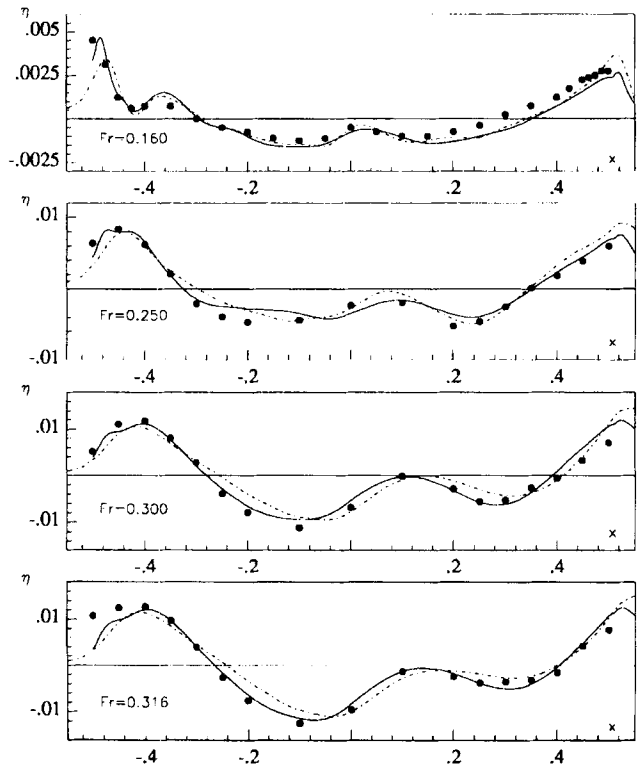

Figure 21. Free surface elevation along the hull: multidomain solution (solid line), potential solution (broken line) and experimental data[26] (symbols) for the S60 free surface flow with $Fr = 0{\cdot}160$, $0{\cdot}250$, $0{\cdot}300$, $0{\cdot}316$

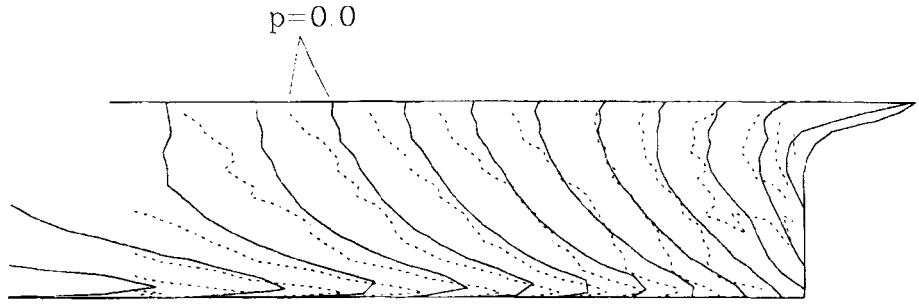

Figure 22. Pressure at the sterm of the S60 hull at $Fr = 0{\cdot}16$: comparison between numerical results (solid line) and experimental data[26] (dashed line). Levels: $-0{\cdot}06$, $-0{\cdot}05$, ..., $0{\cdot}1$

viscous effects, but also to the fact that the boundary condition at the free surface in the viscous domain retains some of its nonlinear features (see (44)).

Finally, the pressure on the hull surface at the stern is compared with measured values at $Fr = 0{\cdot}16$ in Figure 22. Also in this case, the numerical prediction is satisfactory.

The same observations and comments, made in the case of the HSVA tanker with regard to the prediction of the velocity field, hold also in this case (see Figure 23): in fact, the prediction is good up to 90% of the ship length, while near the stern the strong longitudinal vortices observed in the towing tank test are much weaker in the numerical solution.

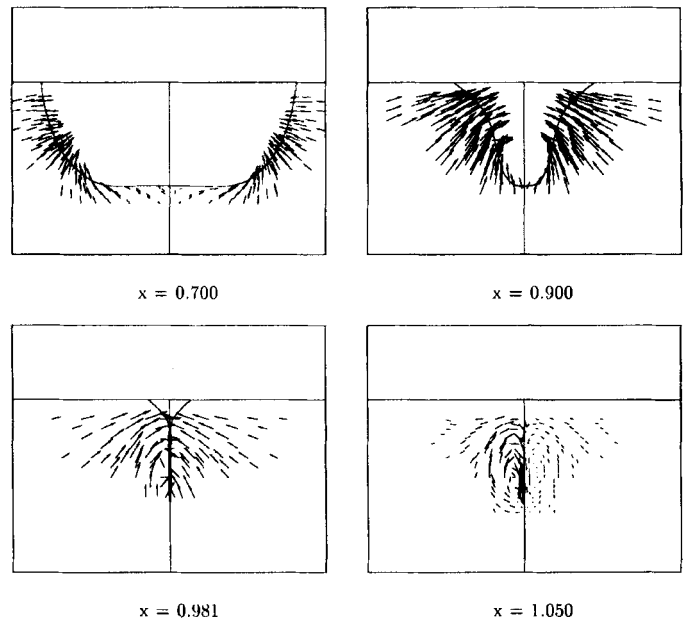

Figure 23. Cross flow velocity vectors: comparison between numerical results (right) and experimental data[25] (left) for the S60 hull $Fr = 0{\cdot}160$ at cross sections $x = 0{\cdot}7$, $0{\cdot}9$, $0{\cdot}981$, $1{\cdot}05$

6. CONCLUDING REMARKS

The numerical solution of a domain decomposition model for free surface steady viscous flows has been obtained; preliminary results are rather encouraging. The coupling algorithm between the viscous and the potential solvers is implemented by a robust iterative scheme. The CPU saving with respect to a full Navier–Stokes code is apparent and promising. Further numerical experiments are needed to analyse the behaviour of the algorithm with more complex ship geometries and the influence of other turbulence models on the prediction of the velocity field in the stern region.

ACKNOWLEDGEMENTS

The work was supported by the Italian Ministry of Merchant Marine in the frame of INSEAN research plan 1988–90.

REFERENCES

1. J. V. Wehausen, 'The wave resistance of ships', *Adv. Appl. Mech.*, 53 (1973).
2. I. Tani, 'History of boundary-layer theory', *A. Rev. Fluid Mech.* **9**, 87 (1977).
3. R. C. Lock and B. R. Williams, 'Viscous–inviscid interactions in external aerodynamics', *Prog. Aerospace Sci.* **24**, 51 (1987).
4. I. Tanaka, 'Three dimensional Ship Boundary Layer and Wake', *A. Rev. Fluid Mech.* **18**, 311 (1986).
5. J. Piquet and M. Visonneau, 'Study of 3D ship boundary layer by means of an inverse method', *Proc. Fourth Int. Conf. on Numerical Ship Hydrodynamics*, Washington D.C., USA, 1985, p. 529.
6. M. Ikehata and Y. Tahara, 'Influence of boundary layer and wake on free surface flow around a ship model', *Nav. Arch. Ocean Eng.*, **26**, 71 (1988).
7. D. Catherall and K. W. Mangler, 'The investigation of the two dimensional laminar boundary layer equations past the point of vanishing skin friction', *J. Fluid Mech.*, **26** 163 (1966).
8. Y. Tahara, F. Stern and B. Rosen, 'An interactive approach for calculating ship boundary layer and wakes for nonzero Froude number', *J. Comp. Physics*, **98**, 33 (1992).
9. C. W. Dawson, 'A practical computer method for solving ship-wave problems', *Proc. Second Int. Conf. on Numerical Ship Hydrodynamics*, Berkeley, USA, 1977, p. 30.
10. F. Lalli, E. Campana and U. Bulgarelli, 'Ship waves computations', *Proc. Seventh Int. Workshop on Water Waves and Floating Bodies*, Val de Reuil, France, 1992, p. 135.
11. E. Campana, A. Di Mascio, P. G. Esposito and F. Lalli, 'Viscous-inviscid coupling in ship hydrodymanics', *Proc. Eleventh Australasian Fluid Mech. Conf.*, Hobart, Australia, 1992, vol. 2, p. 1221.
12. E. Campana, A. Di Mascio, P. G. Esposito and F. Lalli, 'A multidomain approach to free surface viscous flows', *Proc. Eighth Int. Workshop on Water Waves and Floating Bodies*, St John's, Newfoundland, Canada, 1993.
13. E. Campana, A. Di Mascio, P. G. Esposito and F. Lalli, 'Domain decomposition in free surface viscous flows', *Proc. Sixth Int. Conf. on Numerical Ship Hydrodynamics*, Iowa City, 1993.
14. B. S. Baldwin and H. Lomax, 'Thin layer approximation and algebraic model for separated turbulent flows', *AIAA Paper*, 78 (1978).
15. P. Bassanini, U. Bulgarelli, E. Campana and F. Lalli, 'The wave resistance problem in a boundary integral formulation', *Surv. Math. Ind.*, **4**, 151 (1994).
16. D. Kwak, J. L. C. Chang, S. P. Shanks and S. R. Chakravarthy, 'A three-dimensional incompressible Navier–Stokes flow solver using primitive variables', *AIAA J.*, **24**, 390 (1986).
17. A. J. Chorin, 'A numerical method for solving incompressible viscous flow problems', *J. Comput. Phys.*, **2**, 12 (1967).
18. R. M. Beam and R. F. Warming, 'An approximate factorization scheme for the compressible Navier–Stokes equations', *AIAA J.*, **16**, 393 (1978).
19. A. Di Mascio and P. G. Esposito, 'Numerical simulation of viscous flows past hull forms', *The Second Osaka Int. Coll. on Viscous Fluid Dynamics in Ship and Ocean Technology* (1991).
20. Y. Kodama 'Grid generation and flow computation for practical ship hull forms and propellers using the geometrical method and the IAF scheme', *Proc. Fifth Int. Conf. on Numerical Ship Hydrodynamics*, Hiroshima, Japan, 1989, p. 71.
21. H.-C. Chen, W.-M. Lin and K. M. Weems, 'Interactive zonal approach for ship flows including viscous and nonlinear wave effects', *Proc. Sixth Int. Conf. on Numerical Ship Hydrodynamics*, Iowa City, USA (1993).
22. T. Knaack, J. Kux and K. Wieghart, 'On the structure of the flow field on ship hulls', *Osaka Int. Coll. on Ship Viscous Flow*, Japan (1985).
23. L. Larsson, V. C. Patel and G. Dyne, (eds), 'Ship Viscous Flow', *Proc. 1990 SSPA-CTH-IIHR Workshop*, Flowtech International Ab, n. 2, Gothenburg, Sweden (1991).

24. G. B. Deng, P. Queutey and M. Visonneau, 'Navier–Stokes computations of ship stern flows: a detailed comparative study of turbulence models and discretization schemes', *Proc. Sixth Int. Conf. on Numerical Ship Hydrodynamics*, Iowa City, USA (1993).
25. Y. Toda, F. Stern, I. Tanaka and V. C. Patel. *IIHR Report No. 326*, Iowa Institute of Hydraulic Research, The University of Iowa, USA (1988).
26. Y. Toda, F. Stern and J. Longo, *IIHR report No. 352*, Iowa Institute of Hydraulic Research, The University of Iowa, USA (1991).